

The interplay of symmetry and scattering phase in second harmonic generation from gold nanoantennas

Gennaro, Sylvain D; Rahmani, Mohsen; Vincenzo, Giannini; Aouani, Heykel; Sidiropoulos, Themistoklis P H; Navarro-Cia, Miguel; Maier, Stefan A.; Oulton, Rupert F.

DOI:

[10.1021/acs.nanolett.6b02485](https://doi.org/10.1021/acs.nanolett.6b02485)

License:

None: All rights reserved

Document Version

Peer reviewed version

Citation for published version (Harvard):

Gennaro, SD, Rahmani, M, Vincenzo, G, Aouani, H, Sidiropoulos, TPH, Navarro-Cia, M, Maier, SA & Oulton, RF 2016, 'The interplay of symmetry and scattering phase in second harmonic generation from gold nanoantennas', *Nano Letters*, vol. 16, no. 8, pp. 5278-5285. <https://doi.org/10.1021/acs.nanolett.6b02485>

[Link to publication on Research at Birmingham portal](#)

General rights

Unless a licence is specified above, all rights (including copyright and moral rights) in this document are retained by the authors and/or the copyright holders. The express permission of the copyright holder must be obtained for any use of this material other than for purposes permitted by law.

- Users may freely distribute the URL that is used to identify this publication.
- Users may download and/or print one copy of the publication from the University of Birmingham research portal for the purpose of private study or non-commercial research.
- User may use extracts from the document in line with the concept of 'fair dealing' under the Copyright, Designs and Patents Act 1988 (?)
- Users may not further distribute the material nor use it for the purposes of commercial gain.

Where a licence is displayed above, please note the terms and conditions of the licence govern your use of this document.

When citing, please reference the published version.

Take down policy

While the University of Birmingham exercises care and attention in making items available there are rare occasions when an item has been uploaded in error or has been deemed to be commercially or otherwise sensitive.

If you believe that this is the case for this document, please contact UBIRA@lists.bham.ac.uk providing details and we will remove access to the work immediately and investigate.

The interplay of symmetry and scattering phase in second harmonic generation from gold nano-antennas

Sylvain D. Gennaro^{1*}, Mohsen Rahmani^{1*}, Vincenzo Giannini¹, Heykel Aouani¹, Themistoklis P. H. Sidiropoulos¹, Miguel Navarro-Cía², Stefan A. Maier¹, Rupert F. Oulton^{1†}

1. The Blackett Laboratory, Department of Physics, Imperial College London, London SW7 2AZ, UK

2. School of Physics and Astronomy, University of Birmingham, Birmingham B15 2TT, UK

*These authors contributed equally to this work.

†r.oult@imperial.ac.uk

This document includes the following supplementary figures:

1. Experimental setup for nonlinear measurements.
2. Polarisation calibration data for our optical system.
3. SHG of the five configurations for a pump polarized perpendicular to the bar.
4. Comparison of experimental and modelled back focal plane (NA=0.6) images.
5. Electromagnetic simulations of the non-linear polarisation and bright scattering modes at 2ω

This document includes the following supplementary notes:

1. Linear electromagnetic simulations
2. Electromagnetic simulations of the non-linear polarisation and bright scattering modes at 2ω
3. Linear scattering multipole interference model
4. Efficiency of the CIV antenna.

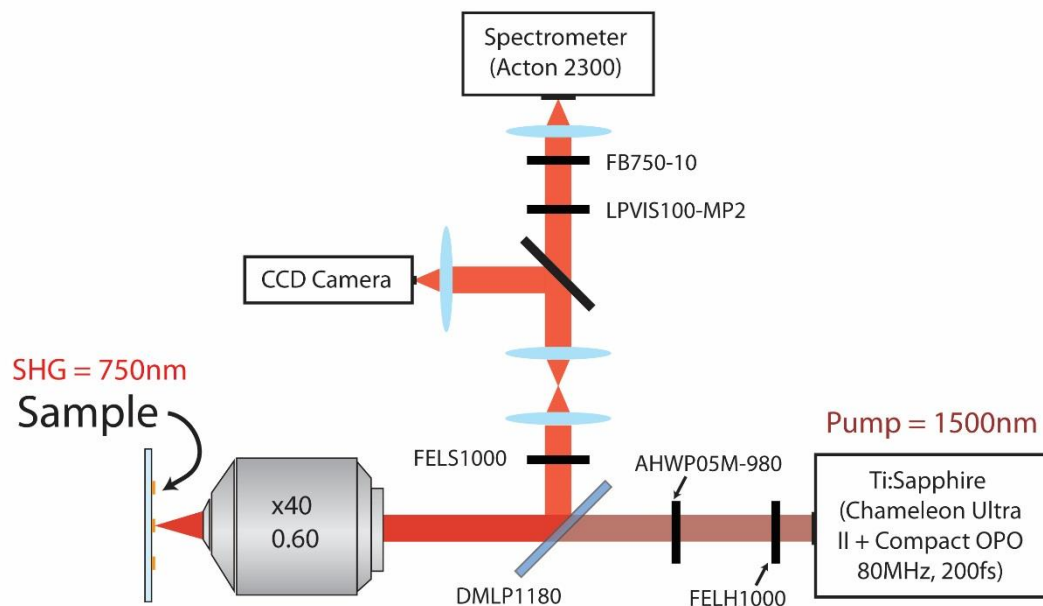


Figure S1. Experimental setup for nonlinear measurements. The second harmonic response from individual optical antennas was generated by focusing a tunable pulsed Ti:Sapphire laser delivering nominally 200 fs pulses at 80 MHz repetition rate with a Nikon S Plan Fluor ELWD 40X 0.6NA microscope objective. The optical antenna acts as a nonlinear element that converts the input signal at a frequency ω into an output signal at the second harmonic 2ω . The collected backward-emitted signal at 2ω is reflected by a dichroic mirror (DMLP1180) to an Acton 2300 Spectrometer. After the sample, the pump is rejected by 1000 nm cut off short pass (FESH1000) and 750 nm bandpass filters (Fb750-10-1, T=60%). (See Methods section from main article for more details.)

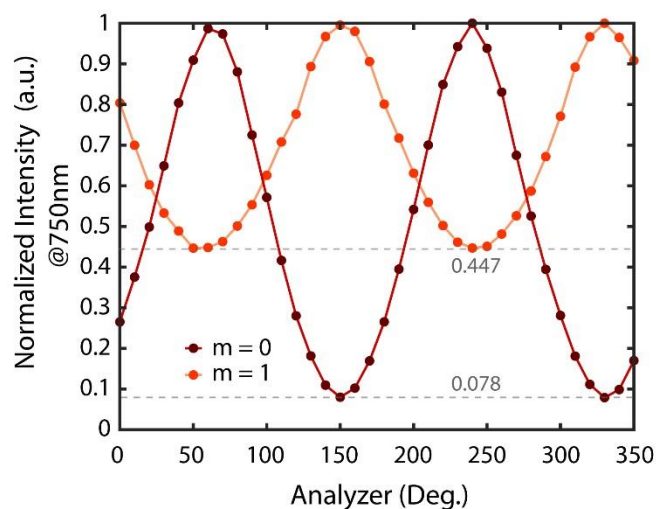


Figure S2. Calibration data to correct for the polarization-dependent detection efficiency of our optical system. Laser pulses at 750 nm were transmitted through the optics and the spectral peak onto the spectrometer are recorded every 10° rotation of a linear polarizer and a constant input laser reference power. In the main article, the back focal plane, resp. the spectral, data are collected at the zero ($m=0$), resp. first ($m=1$), order of our spectrometer. Y (150 deg.) – polarized back focal plane pixel intensities are divided by a correcting factor of 0.078. X (60 deg.) – polarized spectral data are divided by 0.447.

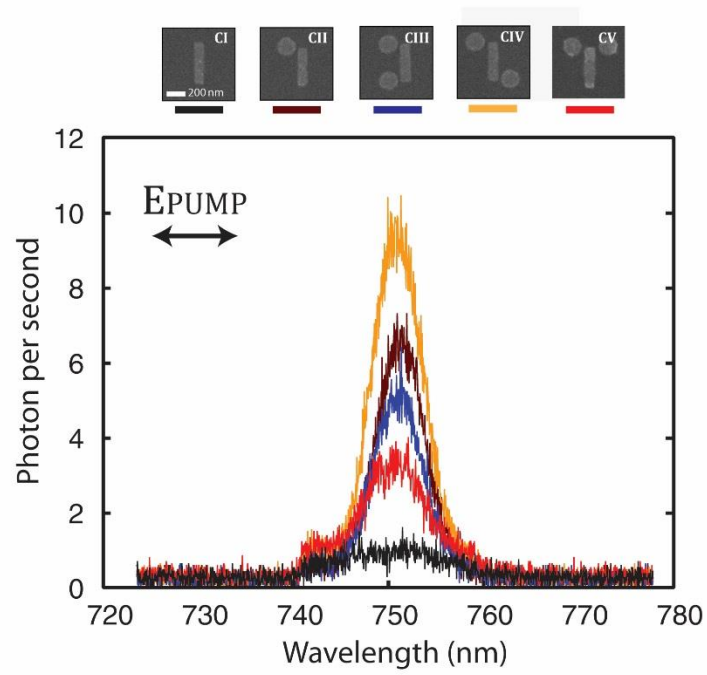


Figure S3. SHG of the five configurations for a pump polarized perpendicular to the bar. Since the bar cannot be excited at the fundamental wavelength of 1,500 nm for this input polarization, the SHG signal is over 3 orders of magnitude weaker than the data for a pump polarized along the bar. Insets are the SEMs of the five nano-antennas explored in the main article.

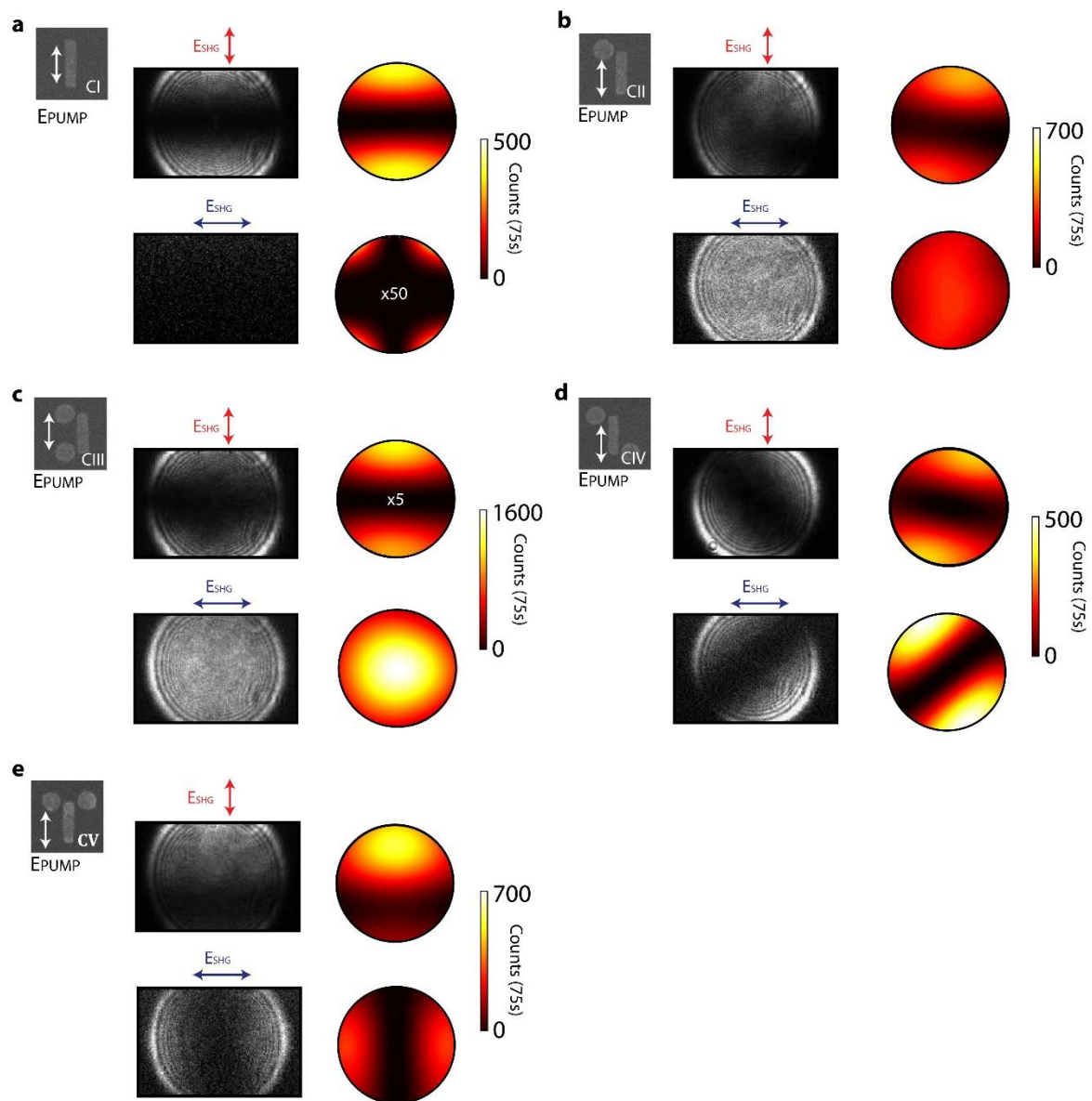


Figure S4. Comparison of experimental and modelled back focal plane (NA=0.6) images for our five configurations (CI to CV). CI models a quadrupole. CII is a combination of 1 dipole and 1 quadrupole. CIII is 2 constructively interfering dipoles and 1 quadrupole. CIV is 2 destructively interfering dipoles and 1 quadrupole. CV is 2 constructively interfering dipole and 1 quadrupole (See Supplementary Note 4). A 2.5deg shift was added to account for an experimental shift of the analyser principal axis with the bar principal axis.

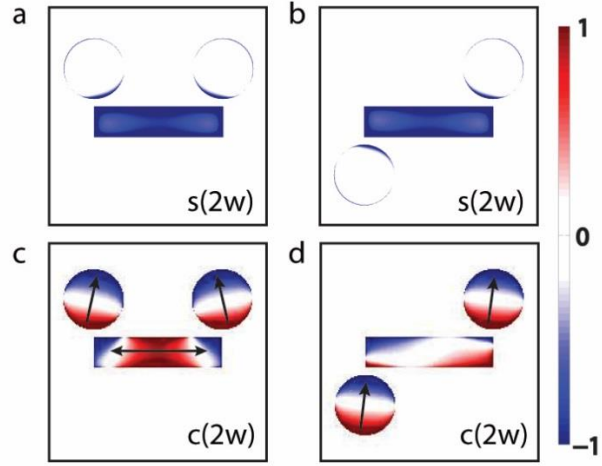


Figure S5. Electromagnetic simulations of the non-linear polarisation and bright scattering modes at 2ω . **a** and **b** show the non-linear surface charge density, $s(2\omega)$, on the air-gold interface generated by the bar particle resonance at ω for CIII and CIV, respectively. $s(2\omega)$ being the source of SHG, couples to modes of the antennas at 2ω . **c** and **d** show the linear charge distributions, $c(2\omega)$, of the antenna modes under normal incidence excitation near the peak extinction at 2ω in Fig. 2c for CIII and CIV, respectively.

Note 1: Linear electromagnetic simulations

The three-dimensional linear electromagnetic simulations of the individual antennas were performed using the three-dimensional finite-difference-time-domain (FDTD) method using the commercial software FDTD solution v8.12 (Lumerical). The nano-antennas were modelled with Au bars of geometrical cross-section $340\text{ nm} \times 80\text{ nm}$ and Au disc of diameter 160 nm lying on a SiO_2 substrate. The dielectric functions of Au and SiO_2 were extracted from the data of Johnson and Christy¹ and Palik², respectively.

Perfect matched layers in all simulation boundaries were used to model a single configuration over a semi-infinite substrate scenario. The solver-defined TFSF source was used to reduce computation effort, as it allows definition of the plane-wave excitation within the volume enclosing only the nano-antennas. The x -polarized plane-wave excitation was incident normal to each configuration from the semi-infinite free space. The incident temporal pulse had central wavelength $1,500\text{ nm}$ and spectral width $\sim 23.65\text{ nm}$ (i.e. pulse length of 140 fs , similar to the 200 fs of the used laser). The solver-defined conformal variant 1 mesh was used to accurately map the details of the model. The larger and smaller cubic grid in the simulation is $20\text{ nm} \times 20\text{ nm} \times 30\text{ nm}$ (outside TFSF source) and $2.5\text{ nm} \times 2.5\text{ nm} \times 0.5\text{ nm}$, respectively. The residual energy in the simulation box volume was at least 50 dB lower than its peak value to ensure that the continuous-wave information obtained by discrete Fourier transformations was valid. A standard convergence test was performed to ensure negligible numerical errors.

Note 2: Electromagnetic simulations of the non-linear polarisation and bright scattering modes at 2ω

In order to gain a deeper understanding of the observations on CIII and CIV, we have simulated the electromagnetic fields at the antenna's ω and 2ω resonances, shown in Supplementary Figure S5. The strength of SHG into a given mode of an antenna depends how the $s(2\omega)$ nonlinear source distribution couples to the mode's linear field distribution. Supplementary Figures S5a and S5b show the distribution of the non-linear surface charge, $s(2\omega)$, on the top air-gold interface of configurations CIII and CIV, respectively. The reader will note that $s(2\omega)$ is symmetric and localized mainly on the bar interface of each antenna, where the electromagnetic field at ω is resonant. The source of SHG is the non-linear surface polarisation vector, $P_i(2\omega)$, within the metal described by the following tensor equation,

$$P_i(2\omega) = \sum_{j,k} \chi_{ijk}^{(2)} E_j(\omega) E_k(\omega)$$

In metals, a second-order nonlinear response is known to arise from a metal's surface^{3,4}, with non-zero second order susceptibility components, $\chi_{\parallel\perp\parallel}^{(2)} = \chi_{\parallel\parallel\perp}^{(2)}$, $\chi_{\perp\parallel\parallel}^{(2)}$ and $\chi_{\perp\perp\perp}^{(2)}$. Here we used the experimental values from Wang et al.⁵ Our numerical study evaluates the corresponding non-linear polarisation charge density, $s(2\omega) = R\{P_{\perp}(2\omega)\}$ on the upper metal surface of the particles, allowing a simplified calculation using only the linear fields from FDTD simulations, $s(2\omega) = R\{\chi_{\perp\perp\perp}^{(2)} E_{\perp}(\omega) E_{\perp}(\omega)\}$.

Supplementary Figures S5c and S5d show the modes of antennas CIII and CIV from our simulation of the extinction at 2ω in Fig. 2c, are shown in Figs. 5c and 5d, respectively, in terms of their linear charge distributions, $c(2\omega)$. Since these modes cause observable normal incidence extinction, they are bright dipole-active modes of the two configurations. The dipolar SHG from CIII is possible because $\sigma(2\omega)$ (Fig. 5a) and $c(2\omega)$ (Fig. 5c) are both symmetric allowing effective coupling whereas dipolar SHG from CIV is forbidden since $\sigma(2\omega)$ (Fig. 5a) and $c(2\omega)$ (Fig. 5c) are not symmetric forbidding effective coupling.

Note 3 – Linear scattering multipole interference model

The model represents each mode of the structure as dipoles that interfere in the far field. For simplicity and emphasis of the experimental result, the description of the geometry does not include modes of higher order than quadrupole, which here is represented as two destructively interfering dipoles⁵.

Since the sizes of our radiative SHG sources (disk and bar) are smaller than the wavelength, we model our system under the electric dipole approximation. We assume the motion of charges to be non-relativistic, and the observation point at a distance \mathbf{r} from the origin is far away from the source ($|\mathbf{r}| \gg \lambda$). In spherical coordinate, $\hat{\mathbf{r}}$, is expressed

by $\hat{\mathbf{r}} = \sin(\theta) \cos(\phi) \hat{\mathbf{x}} + \sin(\theta) \sin(\phi) \hat{\mathbf{y}} + \cos(\theta) \hat{\mathbf{z}}$, where θ is the elevation angle from the z - axis and ϕ is the azimuth angle.

The electric field, $\mathbf{E}(\mathbf{r})$, at a point, \mathbf{r} , from a dipole of polarisation, \mathbf{p} , placed at a distance, \mathbf{s} , from the origin, in the plane $x - y$, is given by⁶:

$$\mathbf{E}(\mathbf{r} - \mathbf{s}) = -\frac{1}{4\pi\epsilon_0} k^2 (\hat{\mathbf{r}}_s \times \mathbf{p} \times \hat{\mathbf{r}}_s) \left\{ \frac{e^{i(\mathbf{k} \cdot |\mathbf{r} - \mathbf{s}|)}}{|\mathbf{r} - \mathbf{s}|} \right\} \quad (1)$$

Where $\hat{\mathbf{r}}_s = \frac{\mathbf{r} - \mathbf{s}}{|\mathbf{r} - \mathbf{s}|}$

Assuming the far field approximation, $|\mathbf{r}| \gg |\mathbf{s}|$ and $\hat{\mathbf{r}}_s \approx \hat{\mathbf{r}}$, this expression can be simplified to

$$\mathbf{E}(\mathbf{r} - \mathbf{s}) = (\hat{\mathbf{r}} \times \mathbf{p} \times \hat{\mathbf{r}}) \left[\frac{1}{4\pi\epsilon_0} k^2 \right] \frac{e^{i(\mathbf{k} \cdot \mathbf{r})}}{|\mathbf{r}|} e^{-i(\mathbf{k} \cdot \mathbf{s})} = \mathbf{E}(\mathbf{r}) e^{-i(\mathbf{k} \cdot \mathbf{s})} \quad (2)$$

We express $\mathbf{E}(\mathbf{r})$ using the field distribution for an interfacial dipole parallel to an interface of refractive index, $n=1.5$, as described by Engheta's formula^{7,8}, and generalised to the case where the dipole is orientated at an arbitrary angle, ϕ_d , compared to the origin.

In a spherical coordinate system,

$$\hat{E}_\theta(\theta, \phi - \phi_d) \propto \left[f(\theta) - \frac{2f(\theta) - 1}{(n^2 - 1)f(\theta) + 1} \sin^2(\theta) \right] \cos(\theta) \cos(\phi - \phi_d) \quad (3)$$

$$\hat{E}_\phi(\theta, \phi - \phi_d) \propto -f(\theta) \sin(\phi - \phi_d) \quad (4)$$

Where

$$f(\theta) = \frac{\cos(\theta)}{\cos(\theta) + \sqrt{n^2 - \sin^2(\theta)}} \quad (5)$$

In our experiment, our back focal planes were measured for x - polarisation or y - polarisation with an analyser at an azimuthal angle, ϕ_{pol} , with respect to the origin axis x . Therefore, we express the spherical vectors (Eq. 3 and Eq. 4) as cartesian vectors $\hat{\mathbf{E}}(\mathbf{r}) = \hat{\mathbf{E}}_x(\mathbf{r}) + \hat{\mathbf{E}}_y(\mathbf{r})$ using the transformation:

$$\begin{pmatrix} E_x \\ E_y \end{pmatrix} = \begin{pmatrix} \cos(\theta) \cos(\phi) & -\sin(\phi) \\ \cos(\theta) \sin(\phi) & \cos(\phi) \end{pmatrix} \begin{pmatrix} E_\theta \\ E_\phi \end{pmatrix} \quad (8)$$

Then, using Jones matrices, we express the electric field after our analyser, $\hat{\mathbf{E}}'(\mathbf{r}) = \hat{\mathbf{E}}'_x + \hat{\mathbf{E}}'_y$ from the electric field E_x and E_y :

$$\begin{pmatrix} E'_x \\ E'_y \end{pmatrix} = \begin{pmatrix} \cos^2(\phi_{pol}) & \cos(\phi_{pol}) \sin(\phi_{pol}) \\ \cos(\phi_{pol}) \sin(\phi_{pol}) & \sin^2(\phi_{pol}) \end{pmatrix} \begin{pmatrix} E_x \\ E_y \end{pmatrix} \quad (11)$$

In the general case of an array of N dipoles \mathbf{p}_n , orientated in the $\mathbf{x} - \mathbf{y}$ plane, at respective positions \mathbf{s}_n from the origin, of respective field amplitude a_n , oscillating with a phase ψ_n , compared to the incident driving electric field (in this work, the nonlinear surface charge polarisation of the bar), the electric field of the dipole array, $\mathbf{E}'(\mathbf{r})$, can be written as,

$$\mathbf{E}'(\mathbf{r}, \theta, \phi) = \sum_{n=1}^N a_n e^{i\psi_n} \mathbf{E}'_n(\mathbf{r}, \theta, \phi - \phi_n) e^{-i(\mathbf{k} \cdot \mathbf{s}_n)} \quad (9)$$

The angular distribution of the average power, \bar{P} , from an arbitrary dipole array is proportional to the square of the electric field,

$$\frac{d\bar{P}}{d\Omega} \propto |\mathbf{E}'(\mathbf{r}, \theta, \phi)|^2 \quad (10)$$

This is the quantity that we will use to fit our back focal and polarisation data.

Numerical parameter fits

The mode of the structure is decomposed as dipoles of polarisation vectors \mathbf{p}_n , $n \in \{1,2,3,4\}$, of amplitude, a_n , at respective vector positions, $\mathbf{s}_n = (x_n, y_n)$, from the origin in a cartesian coordinate. The mode of each disc is represented by a single dipole. The mode of the bar is represented by a quadrupole as two dipoles of opposite orientation (i.e. oscillating out of phase with each other). The position of each dipole is given by the geometry of each structure: dimensions of bars are $340 \times 80 \times 40$ nm in \mathbf{x} , \mathbf{y} and \mathbf{z} , respectively, while discs are of the same thickness with diameters of 160 nm. The gaps between the discs and the bar are 20 nm for all cases. The position of the disc relative to the bar influences the total radiation pattern via adding an additional geometric phase terms $e^{-i(\mathbf{k} \cdot \mathbf{s}_n)}$. This causes the radiation pattern at the back focal plane of our microscope objective to rotate in the plane $\mathbf{x} - \mathbf{y}$ as shown in Fig. 3b (CII) and Fig. 4b (CIV) of the main publication.

Each dipole orientation, ϕ_d , is set with respect to the surface charge nonlinear polarisation of the bar, and it is intuitively set to point inward the bar as supported with the linear simulation at 750 nm of CIII (Supplementary Figure S5). Following this, the model estimates the right angle.

As shown in the main publication, a detuning of the resonance of the disc with respect to the bar adds an extra phase term, $e^{i\psi_n}$. The effect can be seen in the asymmetry of the radiation pattern in CV, and some features in the back focal plane of the structure CII to CIV at different polarisation angles. This will be investigated in another publication.

Finally, a proportional factor relates the back focal plane data (taken at the order zero of our spectrometer) to the polarisation data (taken at the first order) due to the spectrometer different efficiency for the respective polarisation, and variability in the power of the laser system, while a measurement.

In summary, the fitting parameters are:

1. Amplitude of each dipole, a_{di} for the disc and, a_q for the bar.
2. Orientation of each dipole and quadrupole (two opposite dipoles), $\phi_{di,q}$
3. Detuning phase, ψ_{di} .
4. A proportional factor G between the polarisation data and the back focal plane.

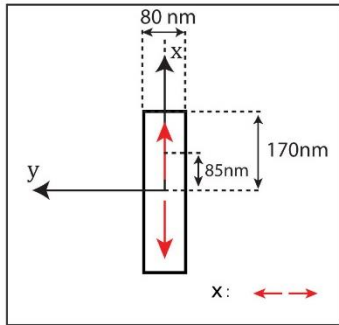
In practice, since the dimension of the bar for each structure (CI to CV), and the input power, should remain the same, we first evaluate the amplitude of quadrupole (two opposite dipoles) of the bar only (CI) and, then, knowing it from the model, we restrict the amplitude of quadrupole in the other structures (CII to CV) to $\pm 15\%$ around this value. It enables us to represent the correct physics. For instance, due to the cancellation of the quadrupole via the two disc's dipoles in CIII, the model underestimates the amplitude of the quadrupole if unbound.

Similarly, since the amplitude of the dipole, a_{di} , is correlated to the dipole orientation, ϕ_{di} , we fix the dipole orientation. Due to the symmetry of each nano-structure, we assume that the angle of the dipole relative to the bar should remain the same for all the different configurations (CII to CV). We select a value of ± 0.34 rad after numerous subsequent fits, and selecting that was appearing more often. In particular, fitting only the back focal plane cross section leads to incorrect polarisation data; there are extremely sensitive to the dipole orientation and are therefore required to estimate it.

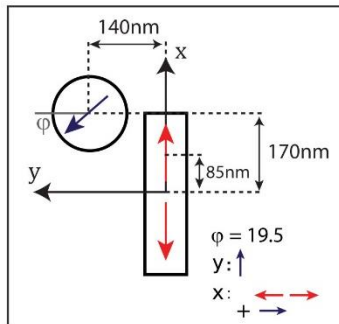
The temporal phase was assume to be positive and to be within 0 and $\frac{\pi}{2}$. The fit gives values ranging from 0.4 to 0.7 rad for the various configurations.

Finally, we round up the parameter to the nearest decimal to account for deviation of the experimental data due to noise, and imperfection of the structure. In our model, a structure is “perfect” if dipole amplitudes of the two discs are equal. In practice, different disc amplitudes are visible with a rotation of the polarisation data, and/or asymmetric radiation pattern as seen in CIV, Fig. 4b. The model is designed primarily to capture the overall physics of each structure, and illustrates how the different phases (of each element contribute to generate the correct back focal plane).

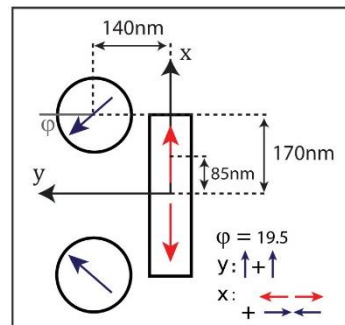
A summary of all the parameters and the dipole orientations given by the model are presented in the table below.



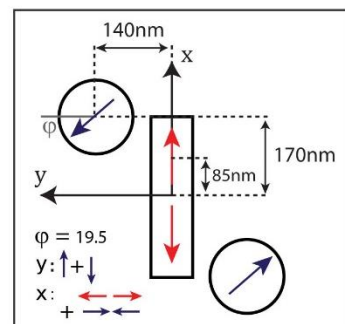
$x_p = [-85, 85]$; X - Position of the dipole (nm)
 $y_p = [0, 0]$; Y - Position of the dipole (nm)
 $p = [95, 95]$; Amplitude of each individual dipole
 $\phi_i = [\pi, 0]$; Orientation of each dipole with respect to the x - axis.
 $\psi_i = [0, 0]$; Temporal phase coupling (rad) relative to the bar
 $G = 7.2 \times 10^{-4}$; Proportional factor between back focal plane data and polarisation.



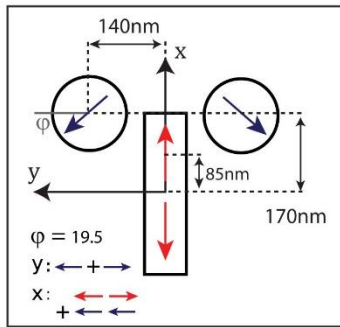
$x_p = [-85, 85, 170]$;
 $y_p = [0, 0, 140]$;
 $p = [105, 105, 47]$;
 $\phi_i = [\pi, 0, \pi/2 + 0.34]$;
 $\psi_i = [0, 0, 0.41]$;
 $G = 7.4 \times 10^{-4}$;



$x_p = [-85, 85, -170, 170]$;
 $y_p = [0, 0, 140, 140]$;
 $p = [95, 95, 53, 53]$;
 $\phi_i = [\pi, 0, \pi/2 - 0.34, \pi/2 + 0.34]$;
 $\psi_i = [0, 0, 0.62, 0.62]$;
 $G = 3.6 \times 10^{-4}$;



$x_p = [-85, 85, -170, 170]$;
 $y_p = [0, 0, -140, 140]$;
 $p = [105, 105, 44, 44]$;
 $\phi_i = [\pi, 0, \pi + \pi/2 + 0.34, \pi/2 + 0.34]$; $\psi_i = [0, 0, 0.7, 0.7]$;
 $G = 6.4 \times 10^{-4}$;



```

xp=[-85,85,170,170];
yp=[0,0,-140,140];
p=[110,110,59,59];
phi=[pi,0,-pi/2-0.34,pi/2+0.34];
psi=[0,0,0.6,0.6];
G=7.2e-4;

```

In summary, the key insights are:

In CI, the main mode of the bar is a quadrupole.

In CII, the disc adds a dipole component along X and Y.

In CIII, the projection of the two dipoles along Y are orientated in the same direction, which leads to in - phase radiation (constructive interferences). Along X, the two dipoles interfere destructively with the quadrupole, which explains the drop of SHG observed.

In configuration CIV, the two dipoles from the disks are orientated in opposite direction, which leads to π out of phase radiation (destructives interferences) in the far field for both X and Y polarisation.

In configuration CV, the two dipoles are out of phase along Y ('dark mode'), and in phase along X. The dipole interferes with the quadrupole, but, due to a detuning phase of 0.6, the radiation pattern is asymmetric.

Supplementary Note 5: Efficiency of the CIV antenna.

The nonlinear coefficient was calculated by taking the ratio of the peak output power divided by the peak input power squared as defined in Ref. ¹⁰. Both peak powers were estimated by including the losses incurred by the spectrometer, the optics and the microscope objective transmission and collection efficiency.

This leads to a non-linear coefficient of:

$$\eta = \frac{P_{out}}{P_{in}^2} > 4.10^{-7}$$

Calculation of P_{in}

Pump Wavelength (m)	λ	1500×10^{-9}
Repetition Rate (Hz)	f	80×10^6
Pulse width (s)	$\Delta\tau$	$>2 \times 10^{13}$
Average Power (W) - 30% transmission efficiency of the microscope objective at 1,500 nm	P_{av}	1.2×10^{-3}
Real NA - The laser beam is smaller than the back aperture so the full NA is not used	NA	0.5
Spot Diameter (m)	$D = 1.22 \frac{\lambda}{NA}$	3.7×10^{-6}
Peak Power (W)	$\frac{P_{av}}{f\Delta\tau}$	<75
Scattering Cross Section / Spot Area. We use the dipole cross section ¹¹	$\frac{3\lambda^2}{4\pi} \frac{1}{\pi(D/2)^2}$	0.05
Input Peak Power (W)	Pin	<3.83

Calculation of P_{out}

The output peak power is calculated taking into account all the various losses due to the spectrometer sensitivity, reflections at various optical surfaces and collection efficiencies of the microscope objective. We have assumed an optimum bright dipole emission of p-polarised due to the bright dipole mode of the disks emitted primarily for this structure.

Total SHG (photons over 75 s): Integrated value of the spectra times. Four photons per count.		3.21×10^{07}
SHG (photons/s)	N_{SHG}	4.28×10^{05}
SHG Average Power (W)	$P_{SHG} = \frac{hc}{\lambda} N_{SHG}$	1.13×10^{-13}
SHG Peak Power (W)	$\frac{P_{SHG}}{f\Delta\tau}$	7.09×10^{-09}
Forward Scattered SHG peak Power (W). Included the transmission loss and the collection efficiency. (n=1.42)	$P_{SHG}^+ = \frac{1}{1 + n_s^3} P_{SHG}$	1.65×10^{-07}
Backward Scattered SHG peak Power (W) - Light that is going through the substrate (n=1.42).	$P_{SHG}^- = \frac{n_s^3}{1 + n_s^3} P_{SHG}$	5.58×10^{-06}
Total Peak Power	P_{out}	7.24×10^{-06}

Losses in the optical system.

This includes the spectrometer efficiency, the transmission of the optical system and the collection efficiency.

Lists of all the detection losses	
Quantum efficiency of the Princeton Excelon Camera	0.8
Cropped – Data as the back focal plane does not fit on the whole CCD array.	0.87
Transmission Efficiency (p - polarized) (Acton SP2300)	0.4
Transmission / Reflection of Optics (4 Lenses plus dichroic mirror)	0.68
Polarizer transmission	0.78
Bandpass Filter	0.6
Transmission microscope objective at 750nm	0.84
Collection efficiency (assume a dipole emission and a Collection angle of $0.6 = 36^\circ$ Solid angle).	0.26
Substrates effect – Silica (refractive index $n=1.5@750\text{nm}$)	0.23
Total	0.0043

Note the loss of approximately 22% due to the transmission (78% @750nm) of the analyser (LPVIS100-MP2 from Thorlabs) should be taken into account when measuring x and y polarisation of the SHG.

References

- (1) Johnson, P. B.; Christy, R. W. *Phys. Rev. B* **1972**, 6 (12), 4370–4379.
- (2) Palik, E. D. *Handbook of Optical Constants.*; ACADEMIC PRESS, 1991.
- (3) Dadap, J. I.; Shan, J.; Heinz, T. F. *J. Opt. Soc. Am. B* **2004**, 21 (7), 1328–1347.
- (4) Capretti, A.; Forestiere, C.; Dal Negro, L.; Miano, G. *Plasmonics* **2014**, 9 (1), 151–166.
- (5) Kujala, S.; Canfield, B. K.; Kauranen, M.; Svirko, Y.; Turunen, J. *Phys. Rev. Lett.* **2007**, 98 (16), 1–4.
- (6) Jackson, J. D. *Classical Electrodynamics*, 3rd ed.; Wiley, 1999.
- (7) Gennaro, S. D.; Sonnefraud, Y.; Verellen, N.; Van Dorpe, P.; Moshchalkov, V. V.; Maier, S. A.; Oulton, R. F. *Nat. Commun.* **2014**, 5 (4748), 3748.
- (8) Engheta, N.; Papas, C. H.; Elachi, C. *Radio Sci.* **1982**, 17 (6), 1557–1566.
- (9) Zhang, S.; Genov, D. A.; Wang, Y.; Liu, M.; Zhang, X. *Phys. Rev. Lett.* **2008**, 101 (047401), 1–4.
- (10) Celebrano, M.; Wu, X.; Baselli, M.; Großmann, S.; Biagioni, P.; Locatelli, A.; De Angelis, C.; Cerullo, G.; Osellame, R.; Hecht, B.; Duò, L.; Ciccacci, F.; Finazzi, M. *Nat. Nanotechnol.* **2015**, 10 (5), 412–417.
- (11) Zumofen, G.; Mojarad, N. M.; Sandoghdar, V.; Agio, M. *Phys. Rev. Lett.* **2008**, 101 (180404), 1–4.